J. Fluid Mech. (2002), *vol.* 456, *pp.* 85–111.
DOI: 10.1017/S002211200100756X Printed in the United Kingdom

On the spatio-temporal stability of primary and secondary crossflow vortices in a three-dimensional boundary layer

By WERNER KOCH

DLR Institut für Aerodynamik und Strömungstechnik, Göttingen, Germany

(Received 29 January 2001 and in revised form 11 October 2001)

To examine possible links between a global instability and laminar–turbulent breakdown in a three-dimensional boundary layer, the spatio-temporal stability of primary and secondary crossflow vortices has been investigated for the DLR swept-plate experiment. In the absence of any available procedure for the direct verification of pinching for three-dimensional wave packets the alternative saddle-point continuation method has been applied. This procedure is known to give reliable results only in a certain vicinity of the most unstable ray. Therefore, finding no absolute instability by this method does not prove that the flow is absolutely stable. Accordingly, our results obtained this way need to be confirmed experimentally or by numerical simulations. A geometric interpretation of the time-asymptotic saddle-point result explains certain convergence and continuation problems encountered in the numerical wave packet analysis. Similar to previous results, all our three-dimensional wave packets for primary crossflow vortices were found to be convectively unstable.

Due to prohibitive CPU time requirements the existing procedure for the verification of pinching for two-dimensional wave packets of secondary high-frequency instabilities could not be implemented. Again saddle-point continuation was used. Surprisingly, all two-dimensional wave packets of high-frequency secondary instabilities investigated were also found to be convectively unstable. This finding was corroborated by recent spatial direct numerical simulations of Wassermann & Kloker (2001) for a similar problem. This suggests that laminar–turbulent breakdown occurs after the high-frequency secondary instabilities enter the nonlinear stage, and spatial marching techniques, such as the parabolized stability equation method, should be applicable for the computation of these nonlinear states.

1. Introduction

The exact mechanism of laminar–turbulent breakdown is still not adequately understood but is of considerable practical importance. A better understanding of the physics behind this mechanism would not only allow more reliable transition prediction but also open novel approaches to transition control. For steady flows with prescribed environmental noise level, transition appears to be more or less fixed at a particular spatial location. When this spatial location is insensitive to low noise levels, breakdown might be linked to the appearance of a locally absolute instability of the flow. Schatz, Barkley & Swinney (1995) speculated in their conclusion that a change from convective to absolute instability is possibly behind the onset of turbulence in spatially periodic channel flow. An absolute instability describes a temporally unstable

wave with zero group velocity. It usually signals the appearance of a so-called *global instability* supporting time-periodic intrinsic oscillations, cf. the review by Huerre & Monkewitz (1990). Here the term global refers to global in space. Being a temporally unstable solution of equations linearized about a steady base flow, a global instability corresponds to a local Hopf bifurcation, cf. Seydel (1994). Assuming homogeneity in the third direction, the direct solution of such two-dimensional eigenvalue problems, is now feasible, cf. Morzyński, Afanasiev & Thiele (1999), or the survey by Theofilis (2001). Floquet theory, used for our secondary stability computations, is a special case of two-dimensional eigenvalue analysis, namely with one spatially periodic dimension. As long as the direction of homogeneity is not the direction in which an absolute–convective transition is possible, the corresponding two-dimensional eigenvalue computations provide an alternative to direct numerical simulations (DNS) for identifying the onset of a global instability.

The absolute instability found by Lingwood (1995, 1996) in the rotating disk problem is an often cited example, and motivated several researchers to look for an absolute instability in the related swept-wing problem, i.e. Oertel & Delfs (1995), Lingwood (1997*b*), Taylor & Peake (1998), Ryzhov & Terent'ev (1998), Taylor & Peake (1999), or the recent experimental investigation of White (2000). However, it soon became clear that the analogy between the rotating disk problem and swept-wing flow is not as close as had been anticipated. Because the rotating disk flow is exactly periodic in the circumferential direction only the radial group velocity has to vanish for an absolute instability to exist. On the other hand, there is no physical reason to assume spanwise periodicity on a swept wing, see Taylor & Peake (1998). This means that one component, for example the streamwise component, of the group velocity may vanish, signalling an absolute instability in this direction. However, this is not sufficient for the existence of a true absolute instability unless the other component of the group velocity vanishes also. The necessary extension of Briggs' method, cf. Briggs (1964), Bers (1975), or Huerre & Monkewitz (1990), to three-dimensional wave packets requires the simultaneous pinching of the Fourier inversion contours in the streamwise and spanwise directions. Bers (1975) made an attempt in that direction, but the final analytical details were presented by Brevdo (1991). None of the researchers mentioned above could find such a double pinching for primary crossflow instabilities in a swept-wing boundary layer. Therefore, as far as we know at present, primary crossflow vortices on a swept wing are convectively unstable, i.e. a disturbance, localized in time and space, will be swept away from the location of its initiation. Convective instability is a precondition for the successful application of spatial marching techniques such as the parabolized stability equation (PSE) approach reviewed by Herbert (1997).

Very often, shortly before breakdown high-frequency instabilities are observed of nonlinearly deformed quasi-streamwise vortices, such as saturated Görtler vortices, cf. Li & Malik (1995) or Bottaro & Klingmann (1996), or Dean vortices, cf. Matsubara & Alfredsson (1998). Further examples are low-speed 'streaks' in velocity boundary layers, cf. Alfredsson & Matsubara (2000) or Andersson *et al.* (2001), and natural convection boundary layers, cf. Jeschke & Beer (2001), or the crossflow vortices in a swept-wing boundary layer, cf. Arnal, Coustols & Juillen (1984), Poll (1985), Kohama, Saric & Hoos (1991), Malik, Li & Chang (1994), Lerche (1997), Malik *et al.* (1999), Kawakami, Kohama & Okutsu (1999), White (2000) or White *et al.* (2001). Such longitudinal vortices produce inflectionally unstable velocity profiles and play a key role in several proposed self-sustaining processes, see for example Waleffe (1997) or Dauchot & Manneville (1997). In addition, recent investigations of swirling jets

and wakes, cf. Delbende, Chomaz & Huerre (1998), Loiseleux, Chomaz & Huerre (1998), Olendraru *et al.* (1999) and Yin *et al.* (2000), demonstrated that such flows can support absolute instabilities, suggesting a link between the onset of a locally absolute instability and the phenomenon of vortex breakdown as a logical extension of the group velocity concept of vortex breakdown advanced by Benjamin (1962) and Tsai & Widnall (1980).

The object of the present study is an investigation of the spatio-temporal stability (complex wavenumber and complex frequency) of primary and secondary crossflow vortices in a three-dimensional boundary layer in order to examine whether a change from convective to absolute instability is possible in crossflow vortices. As pointed out by Huerre (1988), primary and secondary instabilities need not have the same absolute–convective stability character. In their theoretical investigation Koch *et al.* (2000) observed that the wake-like spanwise velocity profiles, caused by the stationary nonlinearly distorted primary crossflow vortices, cf. in particular figure 14 in Koch *et al.* (2000), are not only the origin of secondary instabilities but also make secondary instabilities possible candidates for the occurrence of an absolute instability.

However, there are two complications. First, as noted above, a correct analysis has to consider three-dimensional wave packets. At present no numerical algorithm implementing the two-dimensional pinching criterion of Brevdo (1991) is available. One has to rely on the saddle-point method, originally developed by Benjamin (1961), Criminale & Kovasznay (1962) and Gaster (1968). The saddle-point method has the disadvantage that causality is not satisfied *a priori*. The proof that the inversion contour can be deformed into the steepest descent path through a particular saddle point is no easy task, as demonstrated by Lingwood (1997*a*) for the rotating disk problem. Even for primary instabilities only few absolute–convective stability investigations exist for three-dimensional wave packets. Therefore, in the first part of this paper we perform a saddle-point analysis for the primary crossflow vortices in the DLR swept-plate experiment, confirming their convective instability character. At the same time a geometrical interpretation of the saddle-point condition explains certain convergence problems encountered in the numerical saddle-point continuation analysis.

The second complication concerns secondary instabilities. Although Brevdo & Bridges (1996) provided the mathematical derivation of absolute–convective instability criteria for spatially periodic base flows, practically all applications so far have been limited to model flows using amplitude equations with analytically given dispersion relations, as for example Huerre (1988), Brevdo & Bridges (1996) or Chomaz, Couairon & Julien (1999). These amplitude equations describe secondary instabilities in the vicinity of the primary threshold. Aside from Koch (2000), where preliminary results for secondary crossflow vortices in a strongly nonlinear periodic primary base flow were presented, the only exception known to the author is the paper by Brancher & Chomaz (1997). These authors performed a direct numerical simulation of the asymptotic wave packet initiated by a localized initial disturbance in a spatially periodic shear layer. The corresponding numerical technique for computing the impulse response had been developed by Delbende *et al.* (1998) in their investigation of the spatio-temporal instability of the Batchelor vortex. To our knowledge the present investigation is the first direct application of the theory of Brevdo & Bridges (1996) to a high-amplitude spatially periodic base flow, bringing to light several partly unresolved problems.

One new problem at higher amplitudes of the spatially periodic base flow away from the primary threshold is that usually several secondary instability modes are

amplified. It is still unclear how to identify the physically relevant saddle point(s) in the absence of a pinching proof. Using the latter, this problem has been solved by Brevdo *et al.* (1999) for a related primary instability film-flow problem with only two unstable eigenvalues. Also, Lingwood (1997*a*) addressed this problem in her primary stability investigation of the rotating disk. Furthermore, the necessary high resolution of the nonlinear primary vortices leads to rather large secondary eigenvalue problems and requires time-consuming computations for the corresponding eigenvalues. On account of the prohibitive computer time requirements, and since we could not detect any sign of an absolutely unstable secondary instability, we limited our secondary stability computations to quasi-two-dimensional wave packets propagating mainly along the axis of the nonlinearly distorted stationary primary crossflow vortices.

2. Review of time-asymptotic wave-packet analysis

Before considering the large-time behaviour of primary and secondary wave packets in the linear regime we give a brief review of the corresponding analysis, cf. Briggs (1964), Gaster (1968), Brevdo (1991) or Oertel & Delfs (1996). Using the parallel-flow assumption and neglecting nonlinear terms in the Navier–Stokes equations, when non-dimensionalized with a suitable reference length L_{ref} and reference velocity U_{ref}, a wave packet generated by an initially localized source can be represented by the following inverse Fourier–Laplace integral:

$$\tilde{q}(x,y,z,t) = \frac{1}{(2\pi)^3}\iint_F\int_L \frac{f(y,\alpha,\beta,\omega)}{D(\alpha,\beta,\omega)} \mathrm{e}^{\mathrm{i}(\alpha x+\beta z-\omega t)}\,\mathrm{d}\omega\,\mathrm{d}\alpha\,\mathrm{d}\beta. \tag{2.1}$$

Here $\tilde{q}$ denotes a disturbance velocity and (x,y,z) are Cartesian coordinates with y being normal to the bounding wall; (α,β) are the complex wavenumbers in the (x,z) direction, t is the time, and ω the complex frequency. $D(\alpha,\beta,\omega) = 0$ denotes the dispersion relation for complex α,β and ω. The function $f(y,\alpha,\beta,\omega)$ depends on the details of the initial excitation and boundary conditions, but is of no concern in our time-asymptotic analysis. The Fourier inversion plane F can initially be taken along the strip of analyticity centred around the respective real axes of the complex α- and β-planes, while the Laplace inversion contour L has to be taken in the complex ω-plane above all singularities of the integrand in order to satisfy *causality*.

For three-dimensional wave packets solutions for large time can be obtained by Brevdo's (1991) extension of Briggs' (1964) method, or alternatively by the saddle-point method, cf. Gaster (1968). Brevdo's (1991) extension requires that the Fourier inversion contours are 'pinched' simultaneously by two coalescing spatial branches originating in different half-planes and corresponding to waves propagating in opposite directions, i.e.

$$D(\alpha,\beta,\omega) = \frac{\partial D}{\partial\alpha}(\alpha,\beta,\omega) = \frac{\partial D}{\partial\beta}(\alpha,\beta,\omega) = 0. \tag{2.2}$$

The saddle-point method hinges on the proof that the Fourier inversion contours can be deformed into the steepest descent path without crossing any singularities. Both requirements are difficult to implement for three-dimensional wave packets. For two-dimensional wave packets Briggs' pinching condition can be implemented directly by solving the global, i.e. the whole spectrum, spatial eigenvalue problem for various fixed imaginary parts ω_i of the Laplace inversion contour until pinching is reached.

No corresponding algorithm is available for three-dimensional wave packets. Therefore, practically all investigations of three-dimensional wave packets make use of the

saddle-point method in connection with a continuation procedure starting with the most unstable saddle point. Oertel & Delfs (1995) extended the continuation technique for two-dimensional wave packets, cf. for example Deissler (1987), Brevdo (1995), or appendix B in Brevdo *et al.* (1999), to three-dimensional wave packets. However, without proof of pinching an absolute instability found by this method is not reliable. Neither does finding no absolute instability by this method prove that the flow is absolutely stable. One cannot exclude the possibility that another saddle point exists which might extend the unstable domain of ray velocities, perhaps producing an absolute instability. Brevdo *et al.* (1999) solved a two-dimensional film flow problem by both methods and demonstrated such a failure of the saddle-point continuation method. For an analytically given model dispersion relation this switching to another saddle point, and the corresponding choice of the 'right' saddle point, was also addressed by Conrado & Bohr (1995), see in particular their figure 6. Therefore, a saddle-point approach combined with a continuation procedure starting with the most unstable saddle point gives reliable results only in a certain vicinity of the most unstable ray. Outside this vicinity the results of such a saddle-point tracking could lead to erroneous conclusions.

Contributions to $\tilde{q}(x, y, z, t)$ in (2.1) come from the continuous spectrum as well as from all discrete singularities of the integrand. For large time the contribution from the temporally most unstable wave, given by $D(\alpha, \beta, \omega) = 0$, will dominate the remaining Fourier inversion and can be evaluated asymptotically for $t \to \infty$ by keeping x/t and z/t fixed and applying the method of steepest descent, see Gaster (1968). For $\partial D/\partial\omega \neq 0$ the dominant contribution comes from saddle points of the phase function, i.e.

$$\frac{\partial\omega_r}{\partial\alpha_r}(\alpha, \beta, \omega) = \frac{x}{t} \equiv U, \qquad \frac{\partial\omega_r}{\partial\beta_r}(\alpha, \beta, \omega) = \frac{z}{t} \equiv W, \tag{2.3}$$

together with

$$\frac{\partial\omega_i}{\partial\alpha_r}(\alpha, \beta, \omega) = 0, \qquad \frac{\partial\omega_i}{\partial\beta_r}(\alpha, \beta, \omega) = 0. \tag{2.4}$$

Here the subscripts r and i denote the real and imaginary part. Equations (2.3) and (2.4) express the fact that, instead of temporal instabilities with real wavenumbers, or spatial instabilities with real frequency, we are looking for instabilities with complex wavenumber and complex frequency but real group velocity (U, W). The corresponding asymptotic result for simple saddle points, cf. Gaster (1968) or Brevdo (1991),

$$\tilde{q}(x, y, z, t) \sim \frac{\exp\{\mathrm{i}\,[\alpha\, U + \beta\, W - \omega]\, t\}}{t\left\{\dfrac{\partial^2\omega}{\partial\alpha^2}\dfrac{\partial^2\omega}{\partial\beta^2} - \left[\dfrac{\partial^2\omega}{\partial\alpha\partial\beta}\right]^2\right\}^{1/2}}, \tag{2.5}$$

describes a wave in a frame of reference moving with velocity (U, W). An observer in this frame of reference measures a Doppler-shifted frequency ω_r' and a temporal growth rate ω_i' given by

$$\omega_r' = \omega_r - \alpha_r U - \beta_r W, \qquad \omega_i' = \omega_i - \alpha_i U - \beta_i W. \tag{2.6}$$

The flow is linearly unstable if there exist ray velocity components U and W such that $\omega_i' > 0$. The flow is termed locally absolutely unstable if the velocity corresponding to the relevant laboratory frame, i.e. in most cases $U = W = 0$, lies within the amplified domain $\omega_i' > 0$ bounded by the neutral $\omega_i' = 0$ contour. Otherwise the instability is

locally convectively unstable, cf. Briggs (1964), or the recent reviews by Huerre & Monkewitz (1990) or Huerre & Rossi (1998).

For analytically given dispersion relations equations (2.2) are solved by Newton iteration, cf. for example Chomaz *et al.* (1999). In this connection it is of interest to point out a link to acoustics of sound-absorbing ducts, where one has attenuated waves instead of growing waves. For given acoustic wall impedance, and neglecting finite-length liner effects, the least-damped duct mode determines the sound attenuation per unit length. According to the infinite duct theory of Cremer (1953) maximal sound attenuation per unit length is attained for such liner properties which force the coincidence of the least-damped duct mode with the second-least-damped mode. This corresponds to conditions (2.2). However, in the sound attenuation problem no pinching occurs because both attenuated waves propagate in the same direction, cf. also Tester (1973) or Koch (1977), in particular figure 24 in the latter paper.

For numerically computed dispersion relations, the conditions (2.4) for prescribed spatial growth rates α_i and β_i are used in the saddle-point continuation procedure. Starting with the most amplified ray, initially α_i and β_i are taken to be zero, cf. the procedure outlined in Oertel & Delfs (1995). Then the corresponding ω, as well as α_r and β_r, can be computed via local eigenvalue iteration. For this purpose we extended the Wielandt iteration, cf. Zurmühl (1961, p. 289ff), to complex α, β. We prefer the temporal algorithm because for secondary instabilities a global spatial eigenvalue solver is still too costly. The ray velocity (U, W) can be determined numerically via (2.3) and the corresponding ω_i' follows from (2.6). Then the spatial growth rate α_i and β_i is varied incrementally until the neutral condition $\omega_i' = 0$, or any other prescribed ω_i', is reached. The rest of the neutral curve can be computed by iterative methods.

3. Spatio-temporal analysis of primary crossflow vortices

Before considering the spatio-temporal stability of secondary crossflow vortices in the DLR swept-plate experiment, we investigate the spatio-temporal stability of the corresponding primary crossflow vortices in this section. As a parameter we use the local chordwise distance, which is equivalent to varying the local Reynolds number as defined in (3.1) below. A thorough description of the DLR swept-plate experiment had been given in the recent review by Bippes (1999) and references cited therein, and will therefore be omitted here. In agreement with the corresponding theoretical investigation of Koch *et al.* (2000) we chose the free-stream velocity $Q_\infty^* = 19\,\mathrm{m\,s^{-1}}$ and the effective sweep angle $\varphi_\infty = 42.5^\circ$. The chord length of the plate is $c^* = 0.5\,\mathrm{m}$. Here the asterisk denotes dimensional quantities. A favourable chordwise pressure gradient on the swept plate is induced by a displacement body above the plate. The experimentally obtained pressure distribution c_p is approximated analytically and the corresponding non-similar boundary-layer computation of Koch *et al.* (2000) provides the spanwise-constant steady laminar base flow velocity $\boldsymbol{Q}^* = (U^*, V^*, W^*)$ for the disturbance velocity $\tilde{\boldsymbol{q}}^* = (\tilde{u}^*, \tilde{v}^*, \tilde{w}^*)$. For infinite swept flow the chordwise velocity at the edge of the boundary layer $U_{c,e}^* = Q_\infty^* \cos\varphi_\infty (1 - c_p)^{1/2}$ depends only on the chordwise coordinate x_c^*. Local quantities are chosen as reference quantities, such as the local similarity length $L_{ref}^* = \{\nu^* x_c^* / U_{c,e}^*(x_c^*)\}^{1/2}$, and the local free-stream velocity $Q_{ref}^* = Q_e^*(x_c^*) = \{(U_{c,e}^*)^2 + (W_{c,e}^*)^2\}^{1/2}$; ν^* denotes the kinematic viscosity. Then the local Reynolds number at a fixed x_c^* is defined by

$$Re = Q_{ref}^* L_{ref}^* / \nu^* = \left\{ U_{c,e}^*(x_c^*) x_c^* / \nu^* \right\}^{1/2} / \cos\varphi_s(x_c^*), \tag{3.1}$$

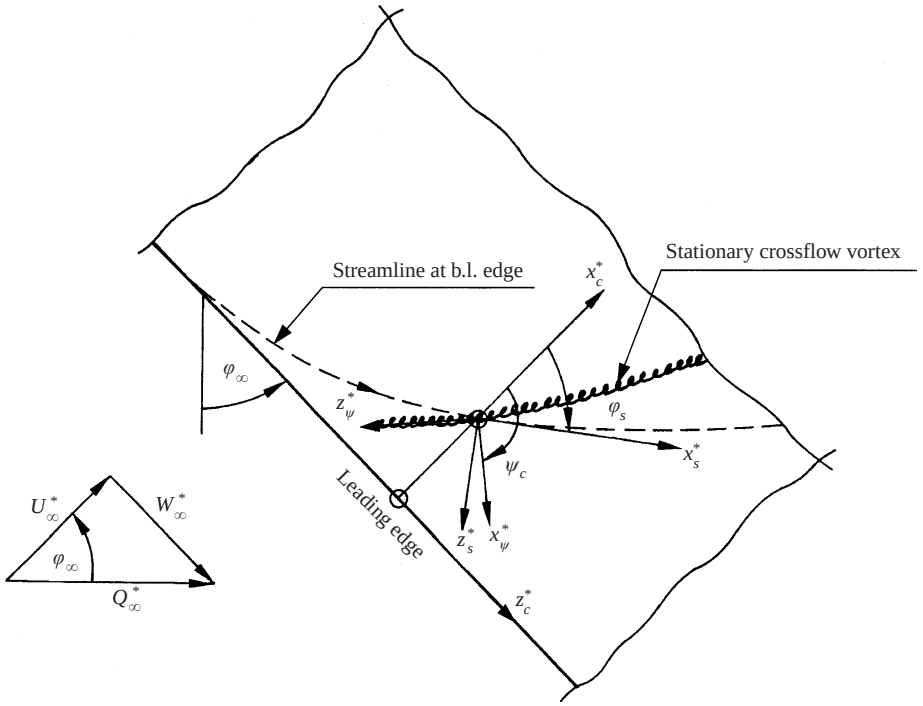

FIGURE 1. Infinite swept plate: coordinate systems.

where φ_s denotes the angle between the chord and free-stream direction at the boundary-layer edge, as sketched in figure 1.

Figure 1 depicts the various coordinate systems used for the swept-plate problem. The body-fixed *chordwise coordinate system* (x_c^*, y^*, z_c^*), is denoted by the subscript c, where x_c^* is in the chordwise direction, z_c^* is in the spanwise direction, and y^* is normal to the plate. Corresponding velocities are denoted by (u_c^*, v^*, w_c^*). For the primary instability analysis often a local *streamwise coordinate system* (x_s^*, y^*, z_s^*), denoted by the subscript s, is employed. Then x_s^* is in the direction of the local free-stream velocity Q_e^* at the boundary-layer edge, and z_s^* is in the crossflow direction normal to x_s^*. For the secondary stability investigation the *wave-oriented coordinate system* $(x_\psi^*, y^*, z_\psi^*)$ is used, where x_ψ^* is in the direction of the primary wave vector $\boldsymbol{k} = (\alpha_c, \beta_c)$ with $\psi_c = \arctan(\beta_c/\alpha_c)$; α_c, β_c are the wavenumbers in the chordwise coordinate system. For the stationary crossflow vortices, treated in this paper, the vortex axis denotes the stationary wave front and the term *vortex-oriented coordinate system* is more appropriate.

As noted in § 2, the spatio-temporal computation begins with real (α, β). Then, conditions (2.4) are satisfied for the global maximum of the temporal growth rate $\omega_{i,max}$ and provide the criterion for linear stability, cf. Drazin & Reid (1981) or Huerre & Monkewitz (1990),

$$\omega_{i,max} > 0 \qquad \text{linearly unstable flow,} \tag{3.2}$$

$$\omega_{i,max} < 0 \qquad \text{linearly stable flow.} \tag{3.3}$$

Following the saddle-point continuation procedure outlined in Oertel & Delfs (1996) we changed the spatial growth rate (α_i, β_i) by a small increment. Keeping the new (α_i, β_i) fixed, we searched again for the maximum of the surface $\omega_i(\alpha_r, \beta_r)$. We continued

Figure	ω_i(contour levels)	ω_i (□)	ω_i (△)
2(*a*)	−0.0208, −0.0205, −0.02038, −0.0202, −0.0198	–	−0.02038
2(*b*)	−0.020, −0.0197, −0.01945, −0.019	−0.01944	–
2(*c*)	−0.0195, −0.0192, −0.019, −0.0185	−0.01840	–
2(*d*)	−0.022, −0.021, −0.0207	–	−0.0209
2(*e*)	−0.0127, −0.0130, −0.0135, −0.0126	–	−0.01261
2(*f*)	−0.0005, 0, +0.0005, +0.001, +0.0015	0.00182	–
4(*a*)	−0.005, −0.001, −0.0006, 0, +0.005, +0.01	0.01159	–
4(*b*)	−0.0025, −0.002, −0.0015, −0.001, 0, +0.0025, +0.005	0.005809	–
4(*c*)	+0.04, +0.0435, +0.044, +0.045	–	0.04356

TABLE 1. ω_i contour levels and value of ω_i at a maximum (□) or saddle-point (△) in figures 2 and 4.

this procedure until the neutral curve $\omega_i' = 0$ in the frame of reference moving with the ray velocities (2.3) was reached. While this continuation procedure worked well for most of the neutral curve, it failed for part of it. To find out the reason behind this failure, we applied the same procedure to the well-studied Blasius boundary-layer flow, and describe the results in the following subsection.

3.1. *Primary wave packet in a Blasius boundary layer*

In various publications Gaster investigated the evolution of a three-dimensional wave packet in a Blasius boundary layer by means of different methods. In his initial theoretical treatment of the time-asymptotic behaviour of three-dimensional wave packets, cf. Gaster (1968), the limited computer capabilities at that time forced Gaster to apply the *real axis approximation*, i.e. he assumed a real dispersion law. Gaster found caustics as a consequence of certain singularities, but showed in Gaster (1981) that these singularities are due to the unrealistic real axis approximation and corrected his earlier results. In the mean time Gaster (1975*b*) used a numerical method to demonstrate quite good agreement between experiment and theory, cf. Gaster (1975*a*), in the linear regime despite the parallel-flow assumption. Spatial DNS by Konzelmann (1990) removed this limitation and extended the results into the nonlinear regime. Recently Chernoray *et al.* (2001) investigated spatio-temporal flow patterns in a straight and weakly swept-wing boundary layer experimentally.

In the following we shall consider only the case at Reynolds number $Re = U^*_\infty L^*_{ref}/\nu^* = 580$, corresponding to the $Re_{\delta^*} = 1000$ example of Gaster (1968). The results are displayed in figure 2. Starting with purely temporal instabilities, i.e. $\alpha_i = \beta_i = 0$, where α, β denote the wavenumbers in the streamwise and spanwise directions, we compute first the maximal temporal amplification $\omega_{i,max}$. In the iso-amplification plot $\omega_i(\alpha_r, \beta_r)$ of figure 2(*f*) the maximum $\omega_{i,max}$ at $(\alpha = 0.15563, \beta = 0)$ is marked by the square symbol. This is also the maximum of ω_i' that can be attained along any ray. The shaded area in figure 2(*f*) indicates the amplified domain $\omega_i > 0$. With (2.3) the ray velocities (U, W) at $\omega_{i,max}(\alpha_i = 0, \beta_i = 0)$ can be computed, essentially providing the propagation velocity of the centre of the wave packet. From (2.6) we obtain the corresponding ω_i', denoted by the square symbol for $W = 0$ in figure 2.

Next, we change the spatial amplification (α_i, β_i) by a small increment. For example, we may choose $\beta_i = 0, \alpha_i = +\Delta\alpha_i$, i.e. procede in the $\arctan \beta_i/\alpha_i = 0^\circ$ direction along the $W = 0$ line. Fixing $\beta_i = 0, \alpha_i = +\Delta\alpha_i$ we compute again the maximum of the new $\omega_i(\alpha_r, \beta_r)$ surface, where condition (2.4) is satisfied. Algorithmically we implemented

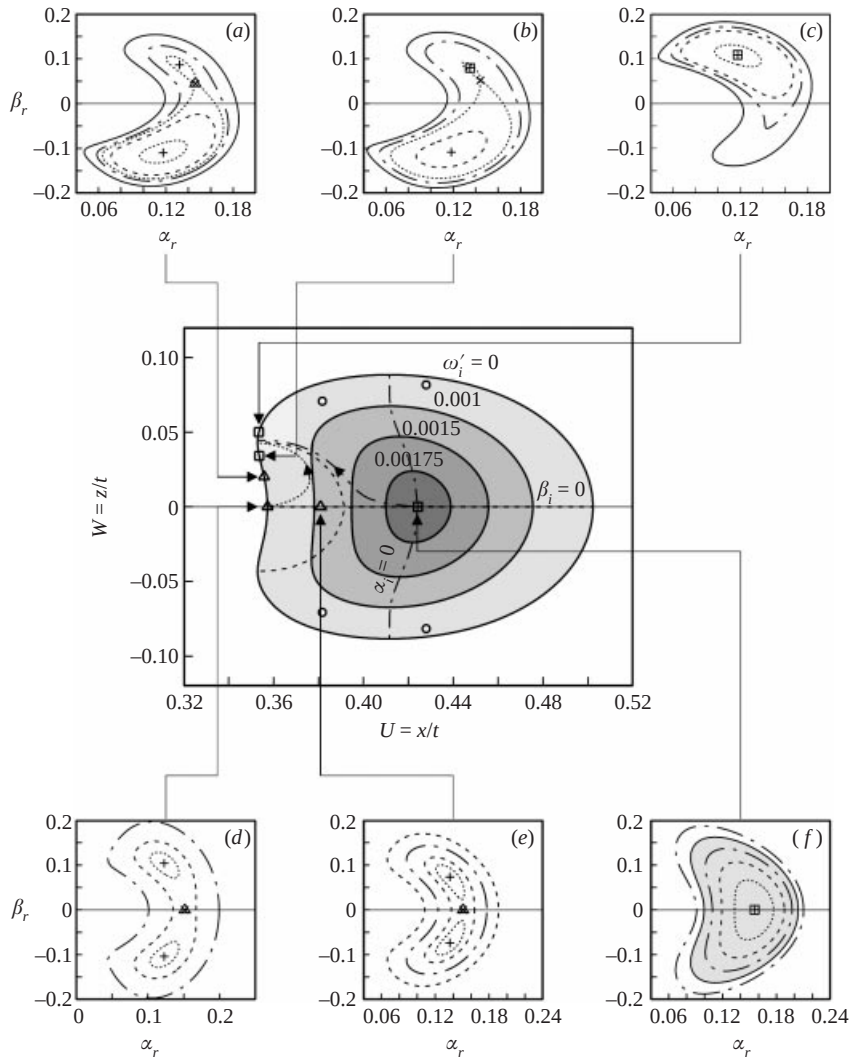

FIGURE 2. Time-asymptotic three-dimensional wave packet in a Blasius boundary layer at $Re = 580$: temporal iso-amplification curves $\omega_i'(U, W) = \text{const.}$ together with six examples (insets *a–c*), of temporal iso-amplification plots $\omega_i(\alpha_r, \beta_r) = \text{const.}$ with (α_i, β_i) fixed. □, a saddle-point condition corresponding to a maximum of the $\omega_i(\alpha_r, \beta_r)$ surface; △, a saddle-point condition corresponding to a saddle point of the $\omega_i(\alpha_r, \beta_r)$ surface. ω_i contour levels are listed in table 1. For comparison the neutral two-dimensional results (○) of figure 3(*a*) are also included.

the search for this maximum by employing a simple gradient method. Increasing α_i further step by step in our saddle-point continuation procedure, we finally reach the neutral point $\omega_i' = 0$ without a problem.

Similarly, we can start our continuation in the opposite direction along $W = 0$ with $\beta_i = 0$ and $\alpha_i = -\Delta\alpha_i$. Near $U \approx 0.39$ we encounter convergence problems in our continuation procedure. A closer look at the corresponding iso-amplification plot $\omega_i(\alpha_r, \beta_r)$ shows that now there are two possibilities where conditions (2.4) are satisfied. The global maximum bifurcates into two maxima with a saddle point in between, cf. the example shown in figure 2(*e*) for $\alpha_i = -0.036, \beta_i = 0$. In figure 2(*e*) the two maxima of the $\omega_i(\alpha_r, \beta_r)$ surface are marked by the two plus symbols. The

saddle point of the $\omega_i(\alpha_r, \beta_r)$ surface at $\alpha_r = 0.15095, \beta_r = 0$, indicated by the triangle in figure 2(*e*), is also a critical point of the $\omega_i(\alpha_r, \beta_r)$ surface and is to be distinguished from the saddle point in the steepest descent method. The saddle-point continuation procedure is no longer unique. Without checking the pinching criterion for three-dimensional wave packets, cf. Brevdo (1991), it is at first not clear which saddle point is the physically relevant one.

Since we are continuing along the symmetry line $W = 0$, the condition $\partial\omega_i/\partial\beta_r = 0$ is satisfied for all $\beta = 0$. Therefore, the solution for two-dimensional wave packets, cf. Brevdo (1995), can be used as guide. For this, the continuation method, as described for example in Appendix B in Brevdo *et al.* (1999), encounters no problem in reaching the neutral point $\omega_i' = 0$, because all saddle points strictly correspond to maxima of the $\omega_i(\alpha_r, \beta_r = 0)$ curve with fixed $(\alpha_i, \beta_i = 0)$. Based on this observation we conclude that for Blasius flow the continuation procedure for three-dimensional wave packets has to switch from computing maxima to computing saddle points of the $\omega_i(\alpha_r, \beta_r)$ surface in order to reach the neutral condition $\omega_i' = 0$ of figure 2(*d*) with $\alpha = 0.15137 - 0.058454\mathrm{i}, \beta = 0$. A direct pinching analysis, which at present is not available for three-dimensional wave packets, would probably lead to the same result. In figure 2 we marked saddle points corresponding to maxima of the $\omega_i(\alpha_r, \beta_r)$ surface by a square symbol, to distinguish them from saddle points corresponding to saddle points of the $\omega_i(\alpha_r, \beta_r)$ surface, marked by triangles. Only the points marked by triangles along $W = 0$ reach the neutral condition for $W = 0$. If one follows the saddle points corresponding to maxima of the $\omega_i(\alpha_r, \beta_r)$ surface, one obtains the dashed curve bifurcating near $U \approx 0.39, W = 0$ in the main figure 2.

Keeping α constant, we may also compute quasi-two-dimensional wave packets in the spanwise direction. The approximate results provide additional support for the physical relevance of our three-dimensional analysis. For example we may fix $\alpha = 0.15563 + 0\mathrm{i}$ at the maximum of figure 2(*f*), marked by the square symbol, and apply the usual two-dimensional saddle-point continuation technique by varying β_i. Similar to the α variation in the streamwise direction with $\beta = 0$ fixed, cf. Brevdo (1995), the global maximum can be continued without difficulty until neutral conditions are reached. The result is shown as curve *f* in figure 3(*a*), where the square symbol corresponds to the square in figure 2(*f*).

Next, we fix $\alpha = 0.15096 - 0.036\mathrm{i}$, corresponding to the saddle marked by the triangle in figure 2(*e*), and again perform a saddle-point continuation in the spanwise direction. The $\omega_i(\beta_r)$ curve for $\beta_i = 0$ in figure 3(*b*) now has two maxima, located symmetrically about $\beta_r = 0$. Furthermore, it has one minimum at $\beta_r = 0$, marked by the triangle. Starting our saddle-point continuation as usual at the maximum, marked by the square symbol in figure 3(*b*), we reach the neutral point by increasing β_i step by step. For each $\beta_i = \text{const.}$ we compute the maximum of $\omega_i(\beta_r)$, proceeding along the thick solid curve in figure 3(*b*). The resulting amplification ω_i' is depicted by curve *e* in figure 3(*a*) to the right of the square. The neutral points in figure 3(*a*) are marked by circular symbols, and are also included in figure 2 for comparison. The definitions (2.3) were used to compute U and W. In this example the two-dimensional approximate results are surprisingly close to the three-dimensional neutral curve.

If we decrease β_i, we see from figure 3(*b*) that this is only possible down to $\beta_i = -0.00114$, denoted by the star symbol. There, the corresponding $\omega_i(\beta_r)$ curve has a vanishing second derivative and $\partial\beta_i/\partial\beta_r = 0$. Therefore, no maximum exists for $\beta_i < -0.00114$. However, minima are also solutions of equations (2.4), and the amplification curve can be continued by finding the minima of $\omega_i(\beta_r)$ along the dotted curve in figure 3(*b*) by increasing β_i until we reach the minimum of the $\beta_i = 0$ curve

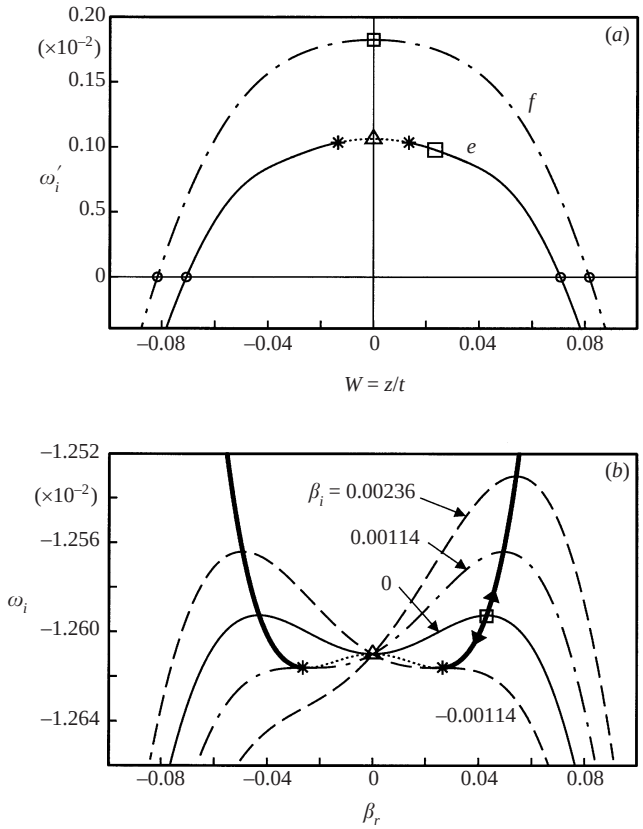

FIGURE 3. Time-asymptotic two-dimensional spanwise wave packets in a Blasius boundary layer at $Re = 580$: (a) growth rate ω_i' as function of spanwise ray velocity W for fixed $\alpha = (0.15563, 0)$ at the maximum in figure 2(f), and fixed $\alpha = (0.15096, -0.036)$ at the saddle in figure 2(e). (b) Saddle-point continuation for fixed $\alpha = (0.15096, -0.036)$ at the saddle in figure 2(e).

marked by the triangle in figure 3(b). The amplification ω_i', corresponding to this continuation of minima, is shown in figure 3(a) by the dotted curve. Concluding, we can say that switching from maxima to saddle points in the three-dimensional saddle-point continuation, corresponds to switching from maxima to minima in the two-dimensional saddle-point continuation, a slight extension of the procedure described in appendix B of Brevdo *et al.* (1999). While this makes our solution more plausible, it is no substitute for a collision check.

To elucidate the saddle-point switching further, we included in figure 2 the dash-dotted curve with the arrow, starting at $\omega_{i,max}$ and giving the results of a saddle-point continuation along $\arctan \beta_i/\alpha_i = 178°$. Only saddle points corresponding to maxima of the $\omega_i(\alpha_r, \beta_r)$ surface are encountered. The dotted curve, originating at $\omega_i' = 0$, $W = 0$, starts with $\arctan \beta_i/\alpha_i = -6°$, and initially corresponds to saddle points of the $\omega_i(\alpha_r, \beta_r)$ surface. In order to reach $\omega_i' = 0$, one has to again switch to computing saddle points corresponding to maxima of the $\omega_i(\alpha_r, \beta_r)$ surface. This switching of the saddle point along the $\omega_i' = 0$ neutral curve is also evident from the iso-amplification plots in figures 2(a)–2(c). For the conditions of figure 2(c), with $\alpha = 0.11751 - 0.053407\text{i}, \beta = 0.10889 + 0.009608\text{i}$, the continuation procedure still follows only maxima of the $\omega_i(\alpha_r, \beta_r)$ surface, starting with the global maximum at $\omega_{i,max}(\alpha_i = 0, \beta_i = 0)$. Near the conditions of figure 2(b), with $\alpha = 0.13498 - 0.054223\text{i}, \beta = 0.07952 - 0.007921\text{i}$,

the switching to the saddle point of the $\omega_i(\alpha_r, \beta_r)$ surface is imminent. In figure 2(a), with $\alpha = 0.14627 - 0.056837\mathrm{i}, \beta = 0.044826 - 0.007728\mathrm{i}$, the saddle-point continuation already follows the saddle points of the $\omega_i(\alpha_r, \beta_r)$ surface.

The conditions (2.4) are only necessary conditions for a maximum or minimum to occur on the $\omega_i(\alpha_r, \beta_r)$ surface. Saddle points, or more degenerate critical points of the $\omega_i(\alpha_r, \beta_r)$ surface also satisfy (2.4). From the theory of functions of several variables it is well known that a sufficient condition for a maximum of $\omega_i(\alpha_r, \beta_r)$ is that additionally $\partial^2\omega_i/\partial\alpha_r^2 < 0$, $\partial^2\omega_i/\partial\beta_r^2 < 0$ and

$$E \equiv \left[\frac{\partial^2\omega_i}{\partial\alpha_r\partial\beta_r}\right]^2 - \frac{\partial^2\omega_i}{\partial\alpha_r^2}\frac{\partial^2\omega_i}{\partial\beta_r^2} < 0. \tag{3.4}$$

$E > 0$ is a sufficient condition for a saddle point on the $\omega_i(\alpha_r, \beta_r)$ surface, while the special case $E = 0$ necessitates the computation of higher derivatives. Such critical points cause computational difficulties. Coincidentally, J. Delfs (personal communication) had also looked at the same test case, but has not published the results. When his Newton iteration did not converge, he extrapolated his results and restarted the Newton iteration with the new starting values. From the geometrical interpretation given above we can see that this meant switching from a maximum to a saddle point of the $\omega_i(\alpha_r, \beta_r)$ surface in the saddle-point continuation procedure. Near the coincidence of a maximum with a saddle point our purely geometrical algorithm, making use of $E > 0$ in searching for a saddle point of the $\omega_i(\alpha_r, \beta_r)$ surface, also fails and a better algorithm, including higher-order derivatives, would be needed.

Figure 2, which should replace the corresponding figure in Gaster (1968) for $Re_{\delta^*} = 1000$, clearly shows that the origin of (U, W) is outside the $\omega_i' = 0$ contour. Therefore, at $Re = 580$ the Blasius boundary layer is locally convectively unstable, as is well known, cf. Gaster (1975b) or Brevdo (1995). If we substitute $x/t = U$, $z/t = W$, the $\omega_i' = 0$ contour also approximates the local spatial structure of the wave packet at $Re = 580$ for large t. Our results for $\omega_i' = 0$ at $Re = 580$ are in complete agreement with unpublished saddle-point continuation results of J. Delfs (personal communication).

From figure 2 we also see that the terminology 'chordwise (or spanwise) absolutely unstable', introduced by Lingwood (1997b) for swept-wedge flows, can be misinterpreted and should be avoided. In a convectively unstable wave packet there will always be the direction normal to the propagation direction of the centre of the wave packet, in which the corresponding group velocity component is zero. Only if both components of the group velocity vanish does it have physical relevance. For example, in the Blasius boundary layer of figure 2 symmetry requires $W = 0$, cf. also figure 3(a), but we do not call this flow 'spanwise absolutely unstable'.

After publication of Koch (2000), I came across the very interesting paper by Conrado & Bohr (1995), in which the origin of non-convex growth shapes $\omega_i'(U, W) = 0$ was studied by means of model equations with analytically given dispersion relations. Looking for the general structure of growth shapes, they also found that global maxima of the $\omega_i(\alpha_r, \beta_r)$ surface can degenerate and include saddle points, with a possible change from one type of solution to the other in order to obtain a well-behaved ω_i' as function of (U, W). This reconfirms the fact that without checking the pinching criterion for three-dimensional wave packets, cf. Brevdo (1991), the results of the saddle-point continuation procedure are not reliable unless physical arguments help in selecting the relevant saddle point.

x_c^*/c^*	α_c	β_c	ψ_c (deg.)	Re	N_p	
0.2	−0.43437	0.24878	150.20	455.4462	8	
0.4	−0.40416	0.30628	142.84	603.4576	8	
0.6	−0.38534	0.34328	138.30	721.1089	10	
0.8	−0.36712	0.37132	134.67	825.5734	12	
(0.9525	−0.35342	0.38906	132.25	899.8744	16	PSE)
1.0	−0.35128	0.39422	131.70	922.3121	16	

TABLE 2. Data of nonlinear steady primary crossflow vortex equilibrium and PSE solution.

3.2. *Primary wave packet in the DLR swept-plate experiment*

Having thus clarified the convergence problem in the numerical saddle-point continuation procedure for Blasius flow, and having validated our code, we procede now with the investigation of the spatio-temporal stability of primary crossflow vortices in the DLR swept-plate experiment, cf. Bippes (1999). For this purpose we chose the wave-oriented coordinate system $(x_\psi^*, y^*, z_\psi^*)$. Since we are discussing only stationary primary crossflow vortices, the term vortex-oriented coordinate system is perhaps more appropriate. Here, x_ψ^* is the coordinate normal to the axis of the nonlinear steady crossflow vortices with a spanwise wavelength of $\lambda_{z_c}^* = 12\,\mathrm{mm}$. This wavelength is close to the experimentally verified maximum amplification of steady crossflow vortices, cf. Koch *et al.* (2000). Coordinate z_ψ^* is then along the vortex axis but in the opposite direction to the growth of the vortex, see figure 1. In order to display the results for primary and secondary crossflow vortices in the same coordinate system, we used the wavenumbers of the nonlinear stationary crossflow vortices, which are slightly different from those for linear stationary crossflow vortices, cf. Koch *et al.* (2000). Some pertinent quantities of interest, namely the chordwise and spanwise wavenumbers with $\psi_c = \arctan(\beta_c/\alpha_c)$, the local Reynolds number and the number of modes N_p retained in the computation of the nonlinear equilibrium solution of the steady crossflow vortices, are listed in table 2 for the five chordwise stations x_c^*/c^* to be investigated.

Sample results of the computations for the time-asymptotic linear three-dimensional wave packet at the chordwise station $x_c/c = 0.4$ are depicted in figures 4 and 5. Again we start our computation with purely temporal instabilities, i.e. $\alpha_{\psi,i} = \beta_{\psi,i} = 0$. For this we compute the maximal temporal amplification $\omega_{i,max}$, marked by the square symbol at $\alpha_\psi = 0.40225, \beta_\psi = -0.05502$ in the iso-amplification plot $\omega_i(\alpha_{\psi,r}, \beta_{\psi,r}) = \text{const.}$ of figure 4(b). Computing (U_ψ, W_ψ) at $\omega_{i,max}(\alpha_{\psi,i} = 0, \beta_{\psi,i} = 0)$ via (2.3) and ω_i' via (2.6), we obtain the point marked by the square symbol in the $\omega_i'(U_\psi, W_\psi)$ plot of figure 4. We fix now for example $\beta_{\psi,i} = 0$ and increase $\alpha_{\psi,i}$ step by step in our saddle-point continuation procedure until we reach $\omega_i' = 0$. This point is marked by the square symbol on the $\omega_i' = 0$ curve in figure 4. The corresponding iso-amplification plot $\omega_i(\alpha_{\psi,r}, \beta_{\psi,r})$, with $\alpha_{\psi,i} = 0.12, \beta_{\psi,i} = 0$, is depicted in figure 4(a) and shows that the corresponding saddle point is at the maximum $\alpha_\psi = 0.21679{+}0.12\mathrm{i}, \beta_\psi = -0.14831{+}0\mathrm{i}$ of the $\omega_i(\alpha_{\psi,r}, \beta_{\psi,r})$ surface. On the other side, in order to reach the point marked by a triangle on the $\omega_i' = 0$ curve by continuation, one has to switch again to computing the saddle point of the $\omega_i(\alpha_{\psi,r}, \beta_{\psi,r})$ surface at $\alpha_\psi = 0.44402{+}0.18546\mathrm{i}, \beta_\psi = -0.03503 - 0.05759\mathrm{i}$, as shown in figure 4($c$). The shaded areas in figures 4(a) and 4(b) again indicate the amplified domain $\omega_i > 0$.

The wavenumbers corresponding to the $\omega_i'(U_\psi, W_\psi)$ curves in figure 4 are depicted

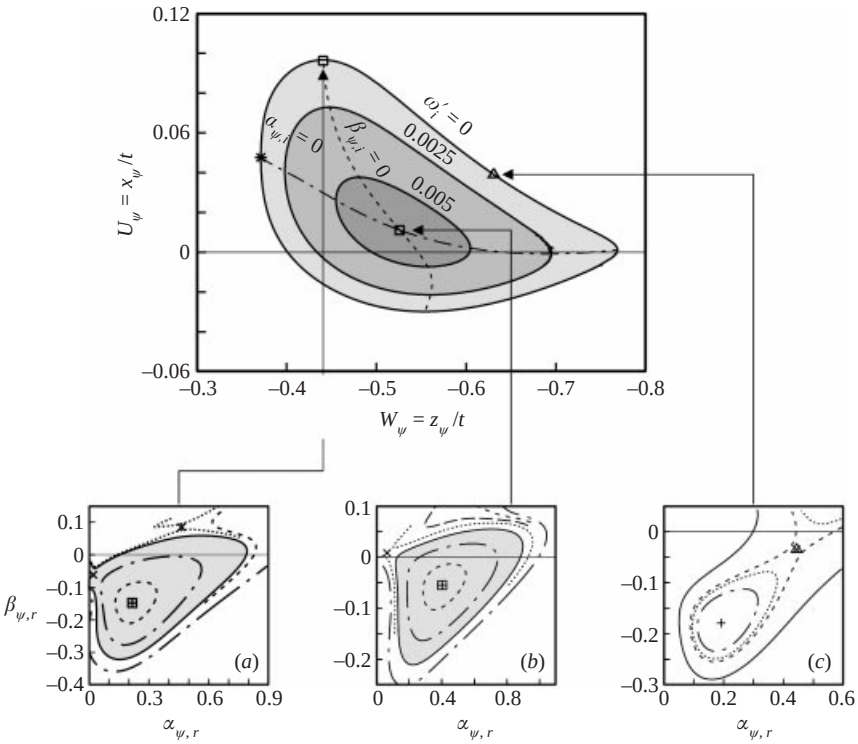

FIGURE 4. Time-asymptotic three-dimensional primary wave packet in the DLR swept-plate experiment at $x_c/c = 0.4$: temporal iso-amplification curves $\omega_i'(W_\psi, U_\psi) = \text{const.}$ together with three examples of temporal iso-amplification plots $\omega_i(\alpha_{\psi,r}, \beta_{\psi,r}) = \text{const.}$ with $(\alpha_{\psi,i}, \beta_{\psi,i})$ fixed. □, *, a saddle-point condition corresponding to a maximum of the $\omega_i(\alpha_{\psi,r}, \beta_{\psi,r})$ surface; △, marks a saddle-point condition corresponding to a saddle point of the $\omega_i(\alpha_{\psi,r}, \beta_{\psi,r})$ surface. ω_i contour levels are listed in table 1.

in figure 5. The same symbols are used to indicate where corresponding points are located. It is interesting to note that the curve $\omega_i'(\alpha_{\psi,i}, \beta_{\psi,i}) = 0$ in figure 5 crosses itself. This means that the same spatial amplification $(\alpha_{\psi,i}, \beta_{\psi,i})$ corresponds to two different points on the neutral $\omega_i' = 0$ curve in figure 4. These are the critical points where the saddle-point continuation procedure switches from maximum to saddle point, or vice versa. Furthermore, we note that due to lack of symmetry the $\alpha_{\psi,i} = 0$ solution of figure 5 no longer corresponds to the two-dimensional wave packet solution $U_\psi = 0$ in figure 4 as for the Blasius boundary layer.

Figure 6 gives a summary of the time-asymptotic results for three-dimensional wave packets at the five chordwise stations $x_c/c = 0.2, 0.4, 0.6, 0.8, 1.0$. This corresponds to the local Reynolds numbers listed in table 2. We see that at all five chordwise stations the neutral $\omega_i' = 0$ curves, bounding the unstable ray velocities, do not include the origin of (U_ψ, W_ψ). Therefore, according to the saddle-point continuation procedure the primary crossflow instabilities in the DLR swept-plate experiment are convectively unstable for these conditions. The vanishing of U_ψ, the group velocity component normal to the vortex axis, is of no importance as long as W_ψ does not vanish simultaneously. The mere fact that the PSE approach worked for the DLR swept-plate flow, cf. Bertolotti (1996) or Koch *et al.* (2000), is already an indication that the primary crossflow vortices in this flow must be convectively unstable.

The spatial shapes of the wave packets in figure 6 look qualitatively similar to

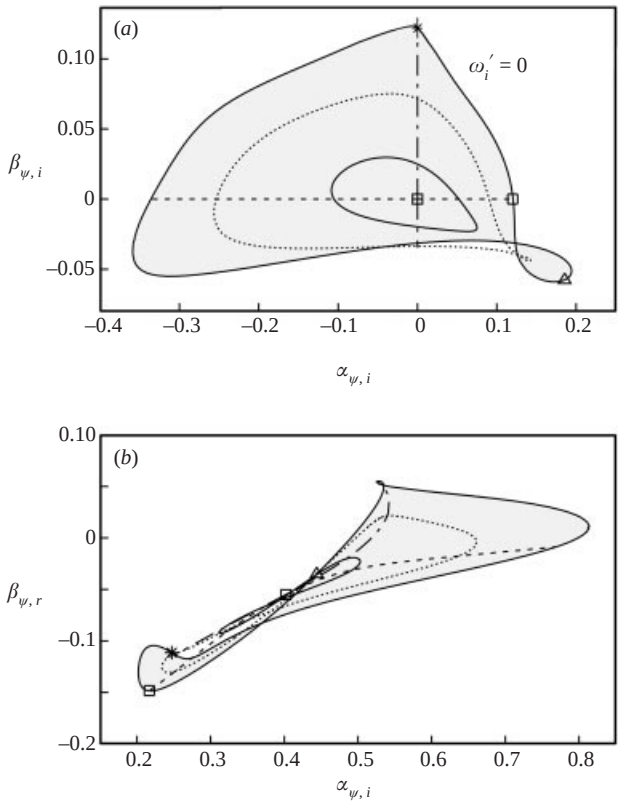

FIGURE 5. Time-asymptotic three-dimensional primary wave packet in the DLR swept-plate experiment at $x_c/c = 0.4$: (*a*) iso-amplification curves $\omega_i'(\alpha_{\psi,i}, \beta_{\psi,i})$ and (*b*) iso-amplification curves $\omega_i'(\alpha_{\psi,r}, \beta_{\psi,r})$ corresponding to the iso-amplification curves $\omega_i'(U_\psi, W_\psi)$ of figure 4. □, ∗, a saddle-point condition corresponding to a maximum of the $\omega_i(\alpha_{\psi,r}, \beta_{\psi,r})$ surface; △, a saddle-point condition corresponding to a saddle point of the $\omega_i(\alpha_{\psi,r}, \beta_{\psi,r})$ surface.

the one computed by Oertel & Delfs (1996) for compressible crossflow vortices on a swept wing. These authors also obtained their results via saddle-point continuation. Therefore, their results are subject to the same limitations with respect to choosing the physically correct saddle point. However, on extending the straight wing and 30° swept-wing experimental investigation of Chernoray *et al.* (2001) to a 45° swept-wing boundary-layer, Pratt *et al.* (2001) recently showed results for spots, which in the linear domain are qualitatively similar to that in figure 6. While this lends some credibility to our saddle-point solutions, it should be emphasized once again that for a proof we still need a practically implementable collision check for three-dimensional wave packets.

4. Spatio-temporal analysis of secondary crossflow vortices

As mentioned in the Introduction, Huerre (1988) recognized very early that the spatio-temporal stability of a secondary instability need not be the same as that for a primary instability. For a secondary instability the amplitude of the nonlinearly deformed primary crossflow vortex becomes an additional parameter. High-frequency secondary instabilities are unstable only above a certain threshold amplitude of the primary crossflow vortex, and have been observed in experiments shortly before tran-

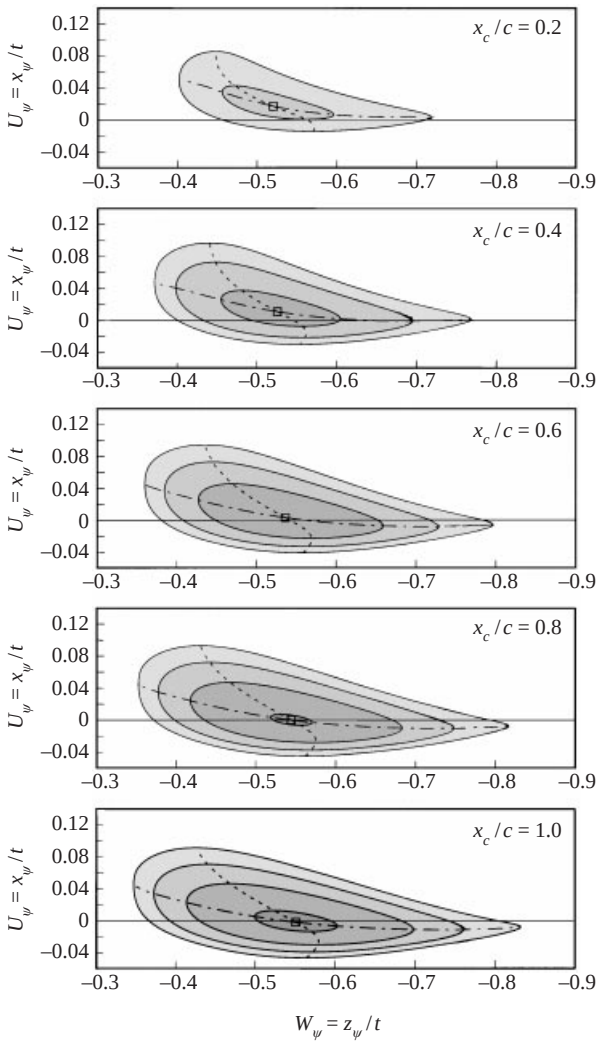

FIGURE 6. Time-asymptotic three-dimensional primary wave packets in the DLR swept-plate experiment initialized at various chordwise stations x_c/c. Temporal iso-amplification contours are shown for $\omega_i' = 0, 0.0025, 0.005, 0.0075$.

sition. For swept-wing and swept-plate flows these have been investigated recently by Malik, Li & Chang (1996), Malik *et al.* (1999), Koch *et al.* (2000), Janke & Balakumar (2000), and in the experiments of Lerche (1997), Kawakami *et al.* (1999), White (2000) and White *et al.* (2001). Very little is known about the spatio-temporal stability of high-frequency secondary instabilities. The preliminary saddle-point results of Koch (2000) for primary steady equilibrium solutions of the DLR swept-plate experiment showed only convectively unstable secondary instabilities up to a chordwise distance $x_c/c = 0.6$. This still left some hope that near the downstream edge of the plate at $x_c/c = 1.0$, where transition is observed experimentally, cf. Deyhle & Bippes (1996), an absolute instability might be found. The main purpose of the present investigation is to fill the gap between $x_c/c = 0.6$ and $x_c/c = 1.0$.

The mathematical theory of absolute–convective instabilities in a spatially periodic base flow was worked out recently by Brevdo & Bridges (1996). Although the proof

is highly intricate, the result for two-dimensional wave packets is extremely simple: by using the Floquet exponent instead of the wavenumber a 'pinching' criterion can be derived completely analogous to the spatially homogeneous case. Thus, neglecting the slow growth of the nonlinear primary steady crossflow vortex along the negative vortex axis z_ψ, i.e. using the parallel flow assumption, and applying Floquet theory, secondary disturbances can be written in the form

$$v(x_\psi, y, z_\psi, t) = \exp\{\mathrm{i}(a_\psi x_\psi + b_\psi z_\psi - \omega t)\} \sum_{\nu=-N_s}^{+N_s} \bar{v}_\nu(y) \exp\{\mathrm{i}\nu\alpha_\psi x_\psi\}. \tag{4.1}$$

Here $\alpha_\psi = (\alpha_c^2+\beta_c^2)^{1/2}$ is the real wavenumber of the primary steady crossflow solution, cf. table 2, and N_s gives the numerical truncation of the secondary modes. In general $N_s = N_p$ with N_p listed in table 2. Also, a_ψ is the complex Floquet exponent, b_ψ the complex wavenumber in the homogeneous direction z_ψ, and ω denotes the complex frequency.

As nonlinear base flow we chose the primary steady crossflow equilibrium solution of Koch *et al.* (2000), because the amplitude of this solution depends only on the chordwise distance x_c/c. However, we note that the equilibrium solution makes use of the parallel-flow assumption and therefore is non-rational. Contrary to this, corresponding parabolized stability equation (PSE) solutions take into account the growth of the crossflow vortices, but depend on the initial conditions, which are governed by receptivity, cf. Malik *et al.* (1996), Stolte (1999) or Koch *et al.* (2000). This is demonstrated in figure 7, which was adapted from figure 7 in Koch *et al.* (2000), and depicts the total disturbance energy E of the steady primary crossflow vortex in the DLR experiment. E is defined per unit mass and non-dimensionalized with the local free-stream velocity and the similarity length in the chordwise direction. It is proportional to the square of the disturbance amplitude. The equilibrium solution essentially envelopes the various PSE solutions, and therefore has been chosen as model for a nonlinear base flow with variable amplitude. The circular symbols mark the chordwise locations of the primary instabilities, investigated in § 3. The triangular symbols show E of the equilibrium solution at the five chordwise stations to be investigated in this section. The star gives E of the primary base flow at the chordwise station of the single PSE case at $x_c/c = 0.95$ to be presented.

In order to find the time-asymptotic solution of a three-dimensional wave packet we have to use the numerically computed dispersion relation for secondary instabilities, and search for saddle points in the (complex) a_ψ- and b_ψ-planes corresponding to a simultaneous 'pinching' of the Fourier inversion contours. As we have seen in § 3, this is already a considerable task for primary instabilities. For secondary instabilities, with more than ten unstable modes, and requiring considerably higher computer times for their computation, this is not yet feasible. We therefore try to get a preliminary idea of the spatio-temporal behaviour of secondary instabilities by investigating quasi-two-dimensional wave packets with $a_\psi = 0$. These two-dimensional wave packets propagate essentially along the axis of the primary vortex. As suggested by a referee one could include variable detuning $a_{\psi,r} \neq 0$ as in figure 17 of Koch *et al.* (2000), and find the wave angle for maximum amplification, cf. also the DNS results of Wassermann & Kloker (2002), but no change in the absolute–convective character would be expected.

A direct computation of the pinching points of such two-dimensional wave packets requires a global eigenvalue solver for spatial secondary instabilities. Due to the large number of secondary modes N_s necessary for convergence, this is orders of

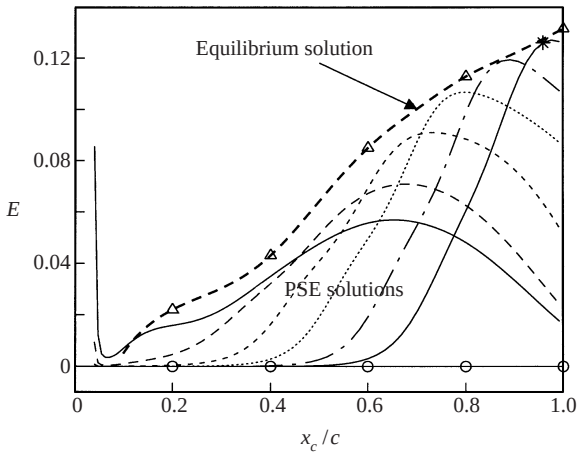

FIGURE 7. Total disturbance energy E of the steady primary crossflow vortex in the DLR swept-plate experiment for $\lambda^*_{z_c} = 12\,\mathrm{mm}$, $Q^*_\infty = 19\,\mathrm{m\,s^{-1}}$ and $\varphi_\infty = 42.5°$, cf. Koch *et al.* (2000). The equilibrium solution envelopes various PSE solutions with initial amplitudes decreasing from left to right. Symbols mark E-values at the chordwise stations of the investigated primary (○) and secondary (△, ∗) instabilities.

magnitude more time consuming than for primary instabilities. Therefore, we use the simpler saddle-point continuation method for the time-asymptotic computation of these quasi-two-dimensional wave packets. Analogous to the procedure for primary instabilities, the starting point is the computation of the maxima $\mathrm{d}\omega_i/\mathrm{d}b_{\psi,r} = 0$ of the temporal amplification rate $\omega_i(b_{\psi,r})$ of all secondary instability modes for $b_{\psi,i} = 0$. To compute the temporal secondary stability we used the v–η formulation described in Koch *et al.* (2000).† For the numerical solution, the truncated Floquet equations, together with the homogeneous boundary conditions, are transformed into an algebraic eigenvalue problem by means of Chebyshev collocation in the wall-normal direction. To obtain sufficient resolution near the boundary-layer edge, where the maxima of the secondary eigenfunctions are expected, a double mapping from Erlebacher & Hussaini (1990) was applied to map the physical domain onto the computational domain. The eigenvalue problem was solved for a few $b_{\psi,r}$ by means of a global solver. Individual eigenvalues for different values of $b_{\psi,r}$ were then computed using Wielandt's iteration, cf. Zurmühl (1961, p. 289ff), extended to complex a_ψ, b_ψ.

Up to $x_c/c = 0.8$ the secondary $\omega_i(b_{\psi,r})$ amplification curves are presented in Koch *et al.* (2000). Figure 8 extends these results for the first few most-amplified modes up to $x_c/c = 1.0$. With increasing amplitude of the primary equilibrium crossflow vortex, corresponding to increasing x_c/c, more and more secondary instability modes become amplified with multiple maxima and even modal coalescence, cf. the case $x_c/c = 0.8$ in figure 8. At least three types of secondary instability modes can be distinguished, denoted by type I, II and III, cf. Malik *et al.* (1996). For all x_c/c the most amplified mode belongs to the type I instability, which is due to inflectional spanwise shear layers, and is marked by solid curves in figure 8. The type II and III instabilities are due to shear layers in the wall-normal direction. Type II modes are depicted by dashed curves. They have their maximum amplitude near the boundary-

† Corrigendum: I am grateful to M. Kloker and R. Messing for pointing out a printing error in Koch *et al.* (2000). In the coefficient $E^{OS}_{\mu,v}$ for $v \neq 0$ on p. 170 the term $-\alpha_{\mu,0}k^2_{\mu,v}$ should be replaced by $-\alpha_{0,v}k^2_{\mu,0}$. All numerical results were obtained with the correct formula.

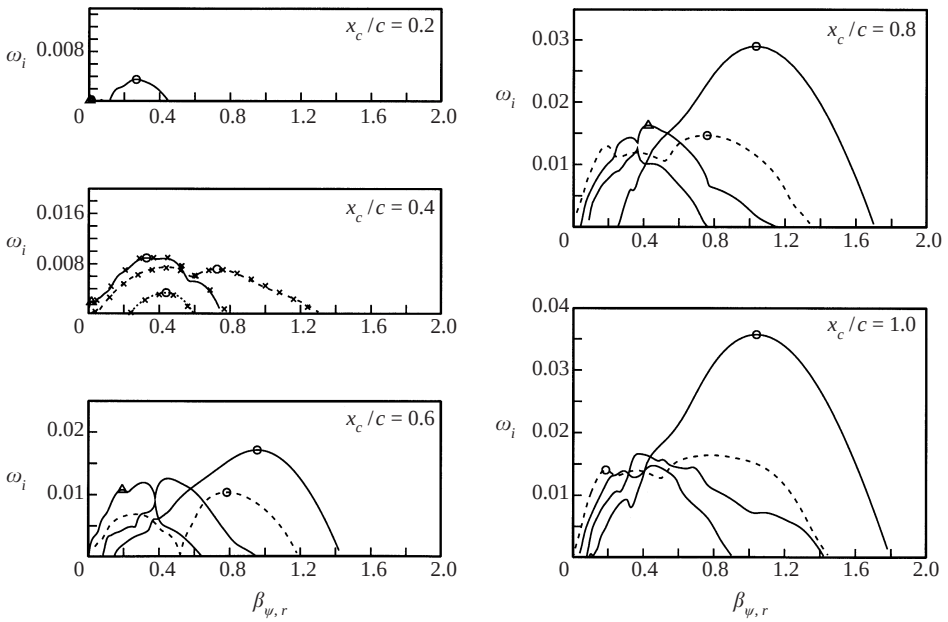

FIGURE 8. Temporal growth rate $\omega_i(b_{\psi,r})$ of secondary instability modes with $a_\psi = 0$ for the primary steady crossflow equilibrium vortex in the DLR swept-plate experiment at various x_c/c; $b_{\psi,r}$ is the wavenumber along the axis of the primary crossflow vortex. Solid, dashed and dotted curves denote, respectively, types I, II and III modes (see text). The symbols $\times$ for $x_c/c = 0.4$ show sample results after doubling the resolution from $N_p = N_s = 8$ to $N_p = N_s = 16$.

layer edge. Type III modes, marked by dotted curves, have their maximum amplitude near the wall. However, modes with lower amplification rates cannot be classified unambiguously.

Using a saddle-point continuation procedure analogous to that employed in § 3 for primary two-dimensional wave packets, we increase or decrease $b_{\psi,i}$ step by step and search for maxima of $\omega_i(b_{\psi,r})$, keeping $b_{\psi,i}$ fixed. Then the corresponding ray velocity W_ψ and amplification ω_i' can be evaluated at the various maxima. This procedure is continued until $\omega_i' = 0$ is reached, as depicted in figure 9 for $x_c/c = 0.4$. The main difference to primary wave packets is that we have several secondary instability modes, and without proof of pinching it is *a priori* not clear which one would be the physically relevant one, cf. the discussion by Conrado & Bohr (1995) or Brevdo *et al.* (1999) for two unstable primary modes. In the following we therefore consider several of the most amplified modes, and check if their group velocity W_ψ approaches zero. In figure 9 the points for $b_{\psi,i} = 0$ correspond to the maxima marked in figure 8 for $x_c/c = 0.4$. They are the starting points of the saddle-point continuation and are denoted by the same symbols. We notice that most of the type I and II modes have group velocities W_ψ close to the boundary-layer edge velocity, and therefore are poor candidates for an absolute instability. It was hoped that the type III mode or modes, with maxima at very low wavenumbers $b_{\psi,r}$ might be better. However, this was not the case for higher x_c/c.

As pointed out by one reviewer, numerical accuracy is questionable if the two-dimensional eigenvalue problem is under-resolved. For the spatio-temporal stability, derivatives of the temporal amplification curves need to be computed, which are even more sensitive to insufficient numerical resolution. This could mean that some

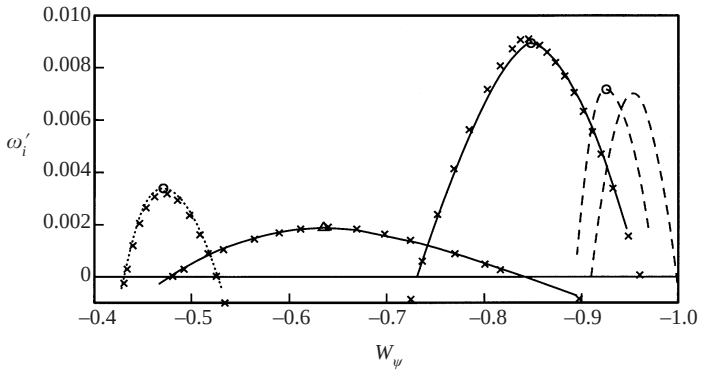

FIGURE 9. Time-asymptotic two-dimensional secondary instability wave packets with $a_\psi = 0$ on the steady primary crossflow equilibrium vortex in the DLR swept-plate experiment at $x_c/c = 0.4$: growth rate $\omega_i'(W_\psi)$ at various saddle points. The symbols $\times$ show the results after doubling the resolution from $N_p = N_s = 8$ to $N_p = N_s = 16$.

of the wiggles in figure 8 are caused by under-resolution and are not physical. In our investigation we had to compromise between accuracy and computer time requirements. Basically we employed the resolution N_p of the equilibrium base flow used in Koch *et al.* (2000), as summarized in table 2, and kept the same number N_s of Floquet modes. While our tests showed that the wall-normal resolution of $K = 55$ Chebyshev polynomials seems adequate in conjunction with the double mapping, the number of Fourier and Floquet modes, i.e. N_p and N_s, is rather low. This is apparent in figure 23 of Malik *et al.* (1996). Increasing the resolution from 8×41 to 16×51 in that paper resulted in noticeable ω_i changes. Therefore, in their recent paper Malik *et al.* (1999) kept 32 Fourier modes, and used the Krylov subspace method to solve the eigenvalue problem.

Following the suggestion of the reviewer, we therefore doubled the resolution for the $x_c/c = 0.4$ case in figure 8 from $N_p = N_s = 8$ to $N_p = N_s = 16$. Sample points of the $N_p = N_s = 16$ computation are included as cross symbols in figure 8. There are visible differences in the temporal growth rate, especially at higher wavenumbers and conditions near a modal coincidence, cf. the high-wavenumber hump in mode I. But in general the accuracy of the temporal growth rate appears to be sufficient for our purpose. Even the low-frequency maximum is predicted accurately. More critical is the accuracy of the saddle points. In figure 9 the results for three modes, computed by doubling the resolution to $N_p = N_s = 16$, are depicted by cross symbols. Comparison with the $N_p = N_s = 8$ curves demonstrates that the domain of unstable ray velocities is accurately predicted with the lower resolution in this example.

Aside from the resolution problem, we should stress the fact that the equilibrium base flow solution is only an approximation due to the quasi-parallel-flow assumption employed. Even higher resolution cannot make it more exact. In this paper we merely use the equilibrium base flow to qualitatively model the effect of increasing base-flow amplitude, in order to explore the possibility of a transition from convective to absolute instability. To estimate how reliable the equilibrium base flow results are, we include a single example using the more realistic PSE base flow. We chose $x_c/c = 0.95$ of the PSE base flow with the lowest initial amplitude depicted in Koch *et al.* (2000), cf. the point marked by the star symbol in figure 7. In his thesis Stolte (1999) had computed such a PSE base flow with $N_p = 16$, and investigated its secondary instability at various chordwise stations. Unfortunately, as discovered

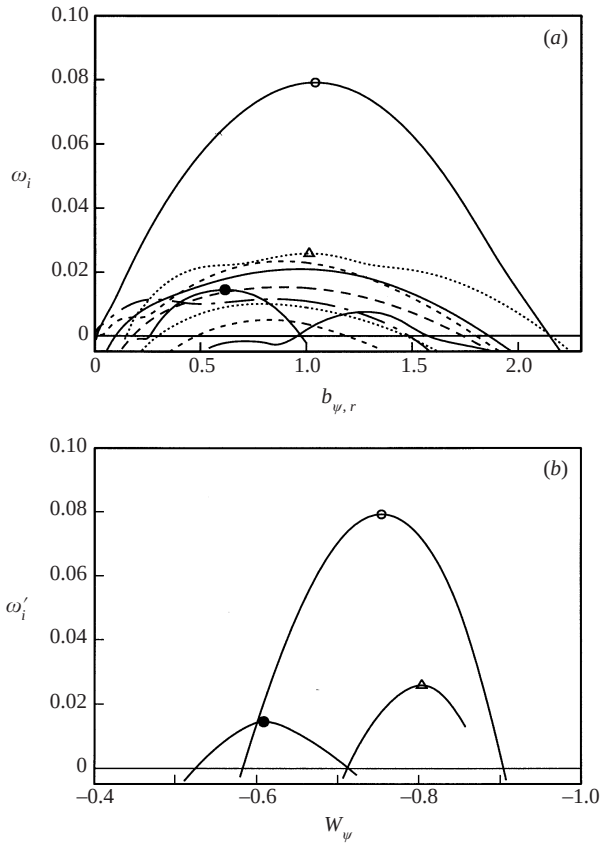

FIGURE 10. PSE base flow at $x_c/c = 0.95$: (*a*) temporal growth rate $\omega_i(b_{\psi,r})$ of the ten most amplified secondary instability modes for $a_\psi = 0$; (*b*) Time-asymptotic two-dimensional secondary instability wave packets propagating along the crossflow vortex axis: growth rate $\omega_i'(W_\psi)$ of the three modes marked by symbols in (*a*).

by Stefan Hein, a small programming error in transforming the PSE base flow from primitive variables to the v–η formulation, makes the secondary stability results in Stolte (1999) quantitatively wrong. With all probability, this also explains the occurrence of modes which did not fit the usual classification of Malik *et al.* (1996). As a consequence, all secondary stability curves had to be recomputed. Figure 10(*a*) shows the recomputed secondary growth rates of the ten most amplified modes for the PSE base flow at $x_c = 0.95$ with $a_\psi = 0$. Qualitative and quantitative differences to the results for the equilibrium base flow are apparent. For example, the secondary amplification rate with the PSE base flow is more than twice as high as that with the equilibrium base flow, even though the total disturbance energy in figure 7 is practically identical. But, in both cases a type I instability is by far the most amplified. Figure 10(*b*) shows wave packet results for three selected modes with $a_\psi = 0$, marked by the same symbols in figure 10(*a*). The amplified domain of the corresponding ray velocities does not include the zero group velocity.

Figure 11 summarizes our results of the saddle-point continuation for the equilibrium base flow with $a_\psi = 0$. For all x_c/c the group velocity W_ψ of the wave packet corresponding to the most amplified mode is around -0.8. In our secondary instability problem we can have more than ten unstable modes. And each mode can

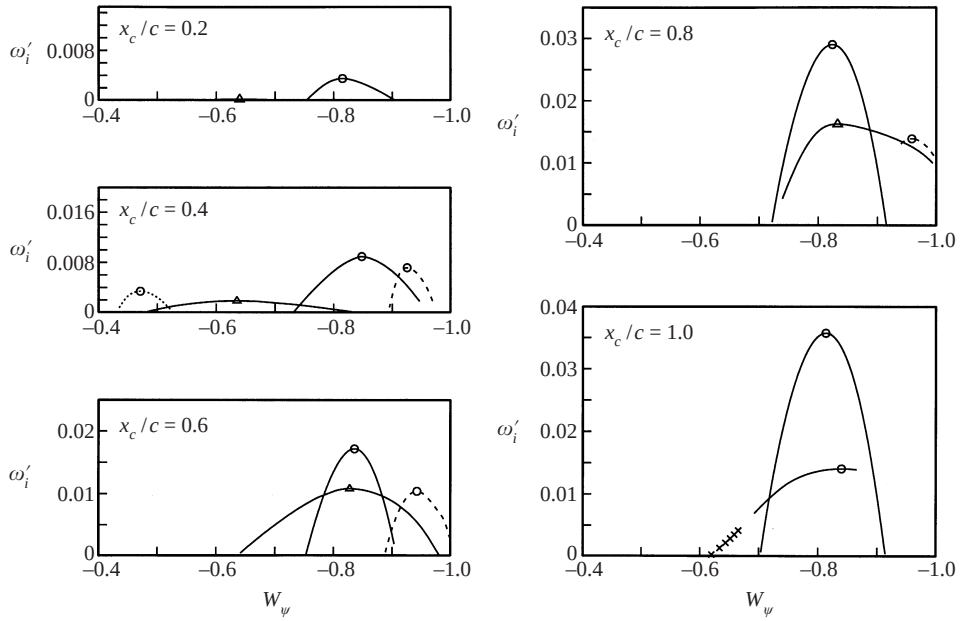

FIGURE 11. Time-asymptotic two-dimensional secondary instability wave packets with $a_\psi = 0$ on the steady primary crossflow equilibrium vortex in the DLR swept-plate experiment: growth rate $\omega_i'(W_\psi)$ of a few selected saddle points at different chordwise stations.

have several maxima and minima. Therefore, without proof of pinching it is not at all clear which saddle point is the physically relevant one, cf. the primary instability analysis of Brevdo *et al.* (1999). Similar to our primary wave packet analysis, the saddle-point continuation of maxima fails at certain points. Then one has to switch from computing maxima to computing minima of the amplification curve $\omega_i(b_{\psi,r})$. The cross symbols in figure 11 for $x_c/c = 1$ are an example of such continuation points for minima. While saddle-point continuation results in continuous ω_i' values at such switching points, ω_i' is discontinuous at modal coincidence points. At present it is not clear if such points have any physical relevance. All we can say with our analysis is that for all saddle points investigated, the amplified ray-velocity domain $\omega_i'(W_\psi) > 0$ did not contain the zero group velocity, i.e. according to saddle-point continuation the secondary high-frequency instabilities in the DLR swept-plate experiment are convectively unstable. However, it must again be emphasized that in the absence of a collision check this is no proof for the non-existence of an absolute instability.

Recent results of a spatial direct numerical simulation (DNS) by Wassermann & Kloker (2001, 2002), for a very similar swept-plate problem strongly support this conclusion. These authors showed that steady disturbances alone result in a steady nonlinear state without transition, similar to the equilibrium solution in Koch *et al.* (2000). When they added a time-periodic background pulse near saturation of the steady disturbances, transition was reached through a strong amplification of high-frequency secondary disturbances. After some simulation time Wassermann & Kloker switched off the periodic background pulse. This caused the unsteady disturbances to be swept downstream and the flow field relaxed again to a steady state, providing clear evidence for the convective nature of high-frequency secondary instabilities. The transient forcing experiment of White (2000), who comes to the same conclusion, is not exactly comparable because with his variable-amplitude leading-edge roughness,

not only the secondary but also the primary disturbance is switched off. But the nonlinear amplitudes of the primary crossflow vortices are a prerequisite for the occurrence of high-frequency secondary instabilities, which might become absolutely unstable. Wassermann & Kloker (2002) correctly retain the almost saturated primary crossflow vortices and only switch off the time-periodic background pulses in their numerical simulation.

5. Conclusion

To examine the possible occurrence of an absolute instability in the three-dimensional boundary layer of the DLR swept-plate experiment we investigated the spatio-temporal stability of primary and secondary instabilities using the parallel flow assumption. The DLR swept-plate experiment constitutes a model for more general three-dimensional boundary layers. For the primary instabilities time-asymptotic three-dimensional wave packets were computed at several chordwise stations corresponding to increasing Reynolds number. We used the saddle-point continuation procedure, starting with the most unstable saddle point, because for three-dimensional wave packets no direct method for the verification of pinching exists at present. As demonstrated in Brevdo *et al.* (1999), finding no absolute instability in the framework of saddle-point continuation does not prove that the flow is absolutely stable. However, unless contrary experimental or DNS evidence exists, these saddle-point results give a first indication about the absolute–convective stability of the flow. A geometric interpretation of the saddle-point continuation elucidated certain convergence problems in the numerical wave packet analysis. However, this is no help in the absence of a verification of the pinching criterion, because there may be other points contributing to the instability which are not connected at all – by any continuation algorithm – to the most unstable saddle point. In agreement with previous findings for similar flows, the saddle-point continuation results for the DLR swept-plate experiment show only convective instability for primary crossflow vortices.

Using the highly nonlinear equilibrium solution for steady primary crossflow vortices as an amplitude-dependent model for a spatially periodic base flow, the second part of this paper applies the recently published theory of Brevdo & Bridges (1996) to study the spatio-temporal stability of high-frequency secondary instabilities. For comparison we also included one example using a PSE base flow. At the higher amplitudes near saturation of the primary crossflow vortices more than ten secondary instability modes are amplified, each with several saddle points. We limited our analysis to quasi-two-dimensional wave packets propagating essentially along the axis of the stationary crossflow vortex. Due to prohibitive CPU time requirements the existing pinching procedure for two-dimensional secondary instabilities cannot be implemented in practice. We applied the saddle-point continuation method again, starting at the maxima of various amplified secondary instability modes. In the absence of a proof of pinching we limit the search to amplified domains of ray velocities which include the zero group velocity. But none of the secondary instability modes investigated came even close to zero group velocity. Again, this does not constitute a proof for the non-existence of an absolute instability, especially since we did not investigate all possible saddle points. But it is an indication that the high-frequency secondary instabilities in the DLR swept-plate experiment are also convectively unstable. This is contrary to our original expectations, because Delbende *et al.* (1998), Olendraru *et al.* (1999) and Yin *et al.* (2000) found parameter regions of absolute instability for the Batchelor vortex, i.e. a longitudinal vortex without bounding walls. Our saddle-point results

were corroborated recently by spatial direct numerical simulations of Wassermann & Kloker (2001, 2002) for a similar three-dimensional boundary layer.

As a consequence of these findings, breakdown to turbulence in a three-dimensional boundary layer is initiated, but not instantly caused, by high-frequency secondary instabilities, cf. Malik *et al.* (1999). Apparently these high-frequency secondary instabilities grow rapidly and reach a nonlinear state before breakdown, as observed experimentally by White (2000), Kohama *et al.* (2000), and White *et al.* (2001). The convective character of secondary instabilities implies that the nonlinear state of secondary instabilities can be computed by means of spatial marching techniques such as the PSE method. Aside from costly spatial DNS, such PSE solutions provide a less time-consuming description of the nonlinear state before breakdown, and possibly give a clue of the breakdown mechanism.

The financial support of the Deutsche Forschungsgemeinschaft, Bonn–Bad Godesberg under the contract Ko 1722/2-2 is gratefully acknowledged. I am grateful to Andreas Stolte and Stefan Hein, not only for many helpful discussions, but especially for providing the PSE base flow and interface to the secondary stability code. Furthermore, I want to thank the Laboratoire J. A. Dieudonné at the Université de Nice Sophia Antipolis for the generous hospitality and stimulating discussions during the final part of this investigation. Last but not least, the critical remarks of two referees led to considerable improvements, and are gratefully acknowledged.

REFERENCES

Alfredsson, P. & Matsubara, M. 2000 Free-stream turbulence, streaky structures and transition in boundary layer flows. *AIAA-Paper* 2000-2534.

Andersson, P., Brandt, L., Bottaro, A. & Henningson, D. 2001 On the breakdown of boundary layer streaks. *J. Fluid Mech.* **428**, 29–60.

Arnal, D., Coustols, E. & Juillen, J. 1984 Experimental and theoretical study of transition phenomena on an infinite swept wing. *Rech. Aerosp.* (4), 275–290.

Benjamin, T. 1961 The development of three-dimensional disturbances in an unstable film of liquid flowing down an inclined plane. *J. Fluid Mech.* **10**, 401–419.

Benjamin, T. 1962 Theory of the vortex breakdown phenomenon. *J. Fluid Mech.* **14**, 593–629.

Bers, A. 1975 Linear waves and instabilities. In *Physique des Plasmas* (ed. C. DeWitt & J. Peyraud), pp. 116–215. Gordon & Breach.

Bertolotti, F. 1996 On the birth and evolution of disturbances in three-dimensional boundary layers. In *Nonlinear Instability and Transition in Three-Dimensional Boundary Layers* (ed. P. Duck & P. Hall), pp. 247–256. Kluwer.

Bippes, H. 1999 Basic experiments on transition in three-dimensional boundary layers dominated by crossflow instability. *Prog. Aero. Sci.* **35**, 363–412.

Bottaro, A. & Klingmann, B. 1996 On the linear breakdown of Görtler vortices. *Eur. J. Mech.* B/*Fluids* **15**, 301–330.

Brancher, P. & Chomaz, J. 1997 Absolute and convective secondary instabilities in spatially periodic shear flows. *Phys. Rev. Lett.* **78**, 658–661.

Brevdo, L. 1991 Three-dimensional absolute and convective instabilities, and spatially amplifying waves in parallel shear flows. *Z. Angew. Math. Phys.* **42**, 911–942.

Brevdo, L. 1995 Convectively unstable wave packets in the Blasius boundary layer. *Z. Angew. Math. Mech.* **75**, 423–436.

Brevdo, L. & Bridges, T. 1996 Absolute and convective instabilities of spatially periodic flows. *Phil. Trans. R. Soc. London* A **354**, 1027–1064.

Brevdo, L., Laure, P., Dias, F. & Bridges, T. 1999 Linear pulse structure and signalling in a film flow on an inclined plane. *J. Fluid Mech.* **396**, 37–71.

Briggs, R. 1964 *Electron-Stream Interaction with Plasmas.* Research Monograph 29, MIT Press.

Chernoray, V., Bakchinov, A., Kozlov, V. & Löfdahl, L. 2001 Experimental study of the K-regime of breakdown in straight and swept-wing boundary layers. *Phys. Fluids* **13**, 2129–2132.

Chomaz, J.-M., Couairon, S. & Julien, S. 1999 Absolute and convective nature of the Eckhaus and zigzag instability with throughflow. *Phys. Fluids* **11**, 3369–3373.

Conrado, C. & Bohr, T. 1995 Growth shapes and turbulent spots in unstable systems. *Phys. Rev.* E **51**, 4485–4502.

Cremer, L. 1953 Theorie der Luftschalldämpfung im Rechteckkanal mit schluckender Wand und das sich dabei ergebende höchste Dämpfungsmaß. *Acoustica* **3**, 249–263.

Criminale, W. & Kovasznay, L. 1962 The growth of localized disturbances in a laminar boundary layer. *J. Fluid Mech.* **14**, 59–80.

Dauchot, O. & Manneville, P. 1997 Local versus global concepts in hydrodynamic stability theory. *J. Phys.* II *Paris* **7**, 371–389.

Deissler, R. 1987 The convective nature of instability in plane Poiseuille flow. *Phys. Fluids* **30**, 2303–2305.

Delbende, I., Chomaz, J.-M. & Huerre, P. 1998 Absolute/convective instabilities in the Batchelor vortex: a numerical study of the linear impulse response. *J. Fluid Mech.* **335**, 229–254.

Deyhle, H. & Bippes, H. 1996 Disturbance growth in an unstable three-dimensional boundary layer and its dependence on environmental conditions. *J. Fluid Mech.* **316**, 73–113.

Drazin, P. & Reid, W. 1981 *Hydrodynamic Stability*. Cambridge University Press.

Erlebacher, G. & Hussaini, M. 1990 Numerical experiments in supersonic boundary-layer stability. *Phys. Fluids* A **2**, 94–104.

Gaster, M. 1968 The development of three-dimensional wave packets in a boundary layer. *J. Fluid Mech.* **32**, 173–184.

Gaster, M. 1975*a* An experimental investigation of the formation and development of a wave packet in a laminar boundary layer. *Proc. R. Soc. Lond.* A **347**, 253–269.

Gaster, M. 1975*b* A theoretical model of a wave packet in the boundary layer on a flat plate. *Proc. R. Soc. Lond.* A **347**, 271–289.

Gaster, M. 1981 Propagation of linear wave packets in laminar boundary layers. *AIAA J.* **19**, 419–423.

Herbert, T. 1997 Parabolized stability equations. *Annu. Rev. Fluid Mech.* **29**, 245–283.

Huerre, P. 1988 On the absolute/convective nature of primary and secondary instabilities. In *Propagation in Systems Far from Equilibrium* (ed. J. E. Wesfreid, H. R. Brand, P. Manneville, G. Albinet & N. Boccara), pp. 340–353. Springer.

Huerre, P. & Monkewitz, P. 1990 Local and global instabilities in spatially developing flows. *Annu. Rev. Fluid Mech.* **22**, 473–537.

Huerre, P. & Rossi, M. 1998 Hydrodynamic instabilities in open flows. In *Hydrodynamics and Nonlinear Instabilities* (ed. C. Godréche & P. Manneville), pp. 81–294. Cambridge University Press.

Janke, E. & Balakumar, P. 2000 On the secondary instability of three-dimensional boundary layers. *Theoret. Comput. Fluid Dyn.* **14**, 167–194.

Jeschke, P. & Beer, H. 2001 Longitudinal vortices in a laminar natural convection boundary layer flow on an inclined flat plate and their influence on heat transfer. *J. Fluid Mech.* **432**, 313–339.

Kawakami, M., Kohama, Y. & Okutsu, M. 1999 Stability characteristics of stationary crossflow vortices in three-dimensional boundary layer. *AIAA-Paper* 99-0811.

Koch, W. 1977 Attenuation of sound in multi-element acoustically lined rectangular ducts in the absence of mean flow. *J. Sound Vib.* **52**, 459–496.

Koch, W. 2000 Absolute/convective instability analysis of secondary cross-flow vortices in a three-dimensional boundary layer. In *Laminar-Turbulent Transition* (ed. H. F. Fasel & W. S. Saric), pp. 601–606. Springer.

Koch, W., Bertolotti, F., Stolte, A. & Hein, S. 2000 Nonlinear equilibrium solutions in a three-dimensional boundary layer and their secondary instability. *J. Fluid Mech.* **406**, 131–174.

Kohama, Y., Alfredsson, P., Egami, Y. & Kawakami, M. 2000 Turbulent energy production mechanism in general boundary layer transition. In *Laminar-Turbulent Transition* (ed. H. F. Fasel & W. S. Saric), pp. 205–210. Springer.

Kohama, Y., Saric, W. & Hoos, W. 1991 A high-frequency, secondary instability of crossflow vortices, that leads to transition. In *Proc. RAS Conf. on Boundary-Layer and Control, Cambridge, UK*, pp. 4.1–4.13.

Konzelmann, U. 1990 Numerische Untersuchung zur räumlichen Entwicklung dreidimensionaler Wellenpakete in einer Plattenrenzschichtströmung. PhD thesis, Universität Stuttgart.

Lerche, T. 1997 Experimentelle Untersuchung nichtlinearer Strukturbildung im Transitionsprozess einer instabilen dreidimensionalen Grenzschicht. *Fortschritt-Bericht VDI Reihe* 7, no 310. VDI-Verlag Düsseldorf.

Li, F. & Malik, M. 1995 Fundamental and subharmonic secondary instability of Görtler vortices. *J. Fluid Mech.* **297**, 77–100.

Lingwood, R. 1995 Absolute instability of the boundary layer on a rotating disk. *J. Fluid Mech.* **299**, 17–33.

Lingwood, R. 1996 An experimental study of absolute instability of the rotating-disk boundary-layer flow. *J. Fluid Mech.* **314**, 373–405.

Lingwood, R. 1997*a* On the application of the Briggs and steepest-descent methods to a boundary-layer flow. *Stud. Appl. Maths* **98**, 213–254.

Lingwood, R. 1997*b* On the impulse response for swept boundary-layer flows. *J. Fluid Mech.* **344**, 317–334.

Loiseleux, T., Chomaz, J. & Huerre, P. 1998 The effect of swirl on jets and wakes: Linear instability of the Rankine vortex with axial flow. *Phys. Fluids* **10**, 1120–1134.

Malik, M., Li, F. & Chang, C.-L. 1994 Crossflow disturbances in three-dimensional boundary layers: nonlinear development, wave interaction and secondary instability. *J. Fluid Mech.* **268**, 1–36.

Malik, M., Li, F. & Chang, C.-L. 1996 Nonlinear crossflow disturbances and secondary instabilities in swept-wing boundary layers. In *Nonlinear Instability and Transition in Three-Dimensional Boundary Layers* (ed. P. Duck & P. Hall), pp. 257–266. Kluwer.

Malik, M., Li, F., Choudhari, M. & Chang, C.-L. 1999 Secondary instability of crossflow vortices and swept-wing boundary layer transition. *J. Fluid Mech.* **399**, 85–115.

Matsubara, M. & Alfredsson, P. 1998 Secondary instability in rotating channel flow. *J. Fluid Mech.* **368**, 27–50.

Morzyński, M., Afanasiev, K. & Thiele, F. 1999 Solution of the eigenvalue problems resulting from global non-parallel flow stability analysis. *Comput. Methods Appl. Mech. Engng* **169**, 161–176.

Oertel Jr., H. & Delfs, J. 1995 Mathematische Analyse der Bereiche reibungsbehafteter Strömungen. *Z. Angew. Math. Mech.* **75**, 491–505.

Oertel Jr., H. & Delfs, J. 1996 *Strömungsmechanische Instabilitäten*. Springer.

Olendraru, C., Sellier, A., Rossi, M. & Huerre, P. 1999 Inviscid instability of the Batchelor vortex: Absolute – convective transition and spatial branches. *Phys. Fluids* **11**, 1805–1820.

Poll, D. 1985 Some observations of the transition process on the windward face of a long yawed cylinder. *J. Fluid Mech.* **150**, 329–356.

Pratt, P., Chernoray, V., Bakchinov, A. & Löfdahl, L. 2001 A quantitative flow visualisation of a point sorce disturbance in a swept wing boundary layer. *EUROMECH Colloquium 423, Stuttgart, April 2–4, 2001.*

Ryzhov, O. & Terent'ev, E. 1998 Streamwise absolute instability of a three-dimensional boundary layer at high Reynolds numbers. *J. Fluid Mech.* **373**, 111–153.

Schatz, M., Barkley, D. & Swinney, H. 1995 Instability in a spatially periodic open flow. *Phys. Fluids* **7**, 344–358.

Seydel, R. 1994 *Practical Bifurcation and Stability Analysis. From Equilibrium to Chaos*, 2nd Edn. Springer.

Stolte, A. 1999 Investigation of transition scenarios in boundary-layer flows. PhD thesis, Georg-August-Universität Göttingen.

Taylor, M. & Peake, N. 1998 The long-time behaviour of incompressible swept wing boundary layers subject to impulsive forcing. *J. Fluid Mech.* **355**, 359–381.

Taylor, M. & Peake, N. 1999 The long-time impulsive response of compressible swept-wing boundary layers. *J. Fluid Mech.* **379**, 333–350.

Tester, B. 1973 The optimization of modal sound attenuation in ducts, in the absence of mean flow. *J. Sound Vib.* **27**, 477–513.

Theofilis, V. 2001 Advances in global linear instability of three-dimensional flows in external and internal aerodynamics. *Prog. Aero. Sci.* (to appear).

Tsai, C.-Y. & Widnall, S. 1980 Examination of a group-velocity criterion for breakdown of vortex flow in a divergent duct. *Phys. Fluids* **23**, 864–870.

Waleffe, F. 1997 On a self-sustaining process in shear flows. *Phys. Fluids* **9**, 883–900.

Wassermann, P. & Kloker, M. 2001 DNS of laminar-turbulent transition in a 3-d aerodynamics boundary-layer flow. In *High Performance Computing in Science and Engineering 2000* (ed. E. Krause & W. Jäger), pp. 275–289. Springer.

Wassermann, P. & Kloker, M. 2002 Mechanisms and control of crossflow-vortex-induced transition in a three-dimensional boundary layer. *J. Fluid Mech.* **456**, 49–84.

White, E. 2000 Breakdown of crossflow vortices. PhD thesis, Arizona State University.

White, E., Saric, W., Gladden, R. & Gabet, P. 2001 Stages of swept-wing transition. *AIAA-Paper* 2001-0271.

Yin, X.-Y., Sun, D.-J., Wei, M.-J. & Wu, J.-Z. 2000 Absolute and convective instability character of slender viscous vortices. *Phys. Fluids* **12**, 1062–1072.

Zurmühl, R. 1961 *Matrizen und ihre technischen Anwendungen*, 3rd Edn. Springer.